

# A Predictive Theory of Electrochemical Ostwald Ripening for Electrodeposited Lithium Metal

Hanning Zhang<sup>†</sup>, Oleg V. Yazyev<sup>†</sup>, and Ruslan Yamaletdinov<sup>†,\*</sup>

<sup>†</sup>Institute of Physics, Ecole Polytechnique Fédérale de Lausanne (EPFL), CH-1015 Lausanne, Switzerland

\*Corresponding author: ruslan.yamaletdinov@epfl.ch

## Abstract

In this work, we present a theoretical framework that describes the evolution of lithium nuclei under the competing effects of electroplating and surface energy-driven redistribution (electrochemical Ostwald ripening). Our model introduces a formulation that accounts for solid electrolyte interphase (SEI) resistance, electrolyte conductivity, and electrode wettability, capturing the transition from SEI to electrolyte-limited growth regimes. We identify asymptotic behaviors for high and low current densities, quantify the conditions under which ripening dominates, and derive analytical expressions for nucleus size, density, and surface coverage. Model predictions show excellent agreement with experimental data across multiple datasets. The results reveal how SEI and electrolyte conductivity, current density and metal-electrode contact angle govern deposition morphology and Coulombic efficiency. Based on these insights, we outline experimentally accessible guidelines to improve battery efficiency and cycling stability - offering a simple yet predictive approach for optimizing metal electrodeposition processes in battery systems and beyond.

## Introduction

The morphology of electrodeposited lithium is a critical factor in the Coulombic efficiency (CE) and lifespan of lithium metal batteries [1]. Irregular deposition, including dendritic and mossy growth, accelerates solid electrolyte interphase (SEI) degradation, increases electrolyte consumption, and raises the risk of short circuits—all of which contribute to battery failure [1–3]. Conversely, smooth and compact lithium deposits improve cycling stability by reducing side reactions and ensuring uniform lithium utilization. Beyond batteries, metal deposition morphology is also critical in general galvanic coatings, where surface roughness and deposit uniformity influence properties such as corrosion resistance, adhesion strength, and electrical conductivity [4]. Understanding the nucleation and growth mechanisms that dictate metal deposition is therefore essential for optimizing both lithium anodes and electroplated coatings.

Following the conventional perspective we divide the metal deposition into two distinct stages: an initial nucleation phase, where new nuclei form and their distribution is established, followed by a growth phase, where existing nuclei expand with minimal additional nucleation [5, 6]. For the former nucleation phase, classical nucleation theory predicts that the probability of forming large nuclei is low due to the  $\sim r^{-2}$  dependence of the Zeldovich coefficient [7]. As a result, under small overpotential  $\eta$  small clusters are initially favored, with a critical radius of  $r^* \sim \frac{2\sigma V_m}{RT}$  ( $\approx 18$  nm for lithium [8]), where  $\sigma$  is the metal/electrolyte surface energy,  $V_m$  is the molar volume,  $T$  is temperature, and  $R$  is the gas constant. Experimentally observed nuclei are however often much larger than this predicted critical size, suggesting that under practical conditions, growth rapidly overtakes nucleation [6].

In classical models, this growth phase proceeds without any dissolution of existing nuclei, and at constant current, is expected to produce a linear increase in nucleus volume,  $r^3 \sim it$ , where  $i$  is current density and  $t$  is time. Yet, contrary to this expectation, several studies have reported a decrease in nucleation density during early stages of deposition [9, 10], implying that smaller nuclei may dissolve over time. This phenomenon is consistent with Ostwald ripening — a redistribution process driven by surface energy minimization, wherein larger nuclei grow at the expense of smaller ones [11, 12] (See Fig 1(a)). Although electrochemical Ostwald ripening has not been explicitly reported in lithium-based systems, it is widely observed in other metal electrodeposition processes — including sodium-ion batteries [13–15], where the ripening promotes the formation of smoother, denser metal layers. In contrast, direct nucleus coalescence - or lithium growth in the form of SEI-passivated

columns [16] - can lead to the trapping of SEI fragments or electrolyte voids, negatively impacting deposit uniformity [17] (See Fig 1(c)). The extent to which Ostwald ripening influences lithium morphology depends on the balance between redistribution and electroplating rates, making ion mobility and surface energy among key parameters in controlling deposit evolution. Despite its evident importance, a quantitative theory for constant plating current has not yet been derived .

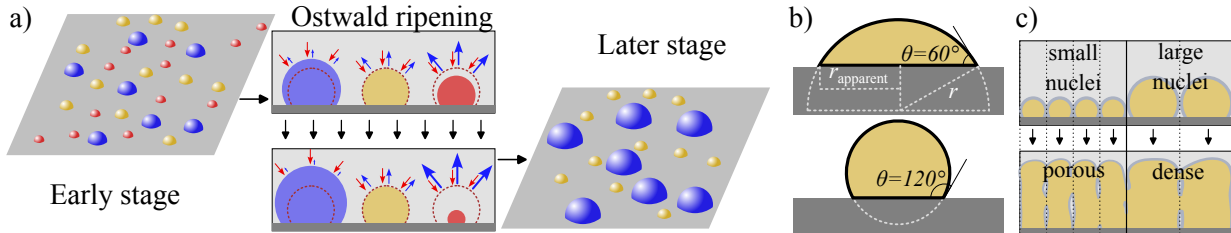


Figure 1: **Schematic overview of Ostwald ripening, nucleus shape effects, and plating uniformity.** a) Ostwald ripening progression: Over time, smaller lithium nuclei dissolve (red) while larger nuclei grow (blue), reducing nucleation density. Yellow nuclei represent stable nuclei of size  $r_s$ , which may evolve over time. b) Impact of contact angle ( $\theta$ ) on nucleus shape: For the same nucleus volume, a higher contact angle ( $\theta = 120^\circ$ ) results in a smaller nucleus with reduced surface coverage, while a lower contact angle ( $\theta = 60^\circ$ ) leads to a wider nucleus. The top panel highlights the nucleus radius  $r$  and the apparent nucleus radius  $r_{\text{apparent}} = \alpha(\theta)r$  ( $\alpha = 1$  for  $\theta \geq 90^\circ$ , and  $\alpha = \sin \theta$  for  $\theta < 90^\circ$ ). c) Effect of nucleus size on lithium plating density: Small nuclei lead to porous, uneven lithium plating, whereas large sparse nuclei facilitate dense, uniform deposition.

A final key parameter determining lithium morphology is electrode wettability, characterized by the metal-electrode contact angle ( $\theta$ ). Wettability affects the surface-to-volume ratio of nuclei, impacting both their shape and deposition uniformity [8, 18, 19]. A lower contact angle promotes lithium spreading, leading to larger nuclei surface, which reduces the probability of dendritic growth and enhances battery longevity [18, 19]. In contrast, lithiophobic surfaces promote localized lithium accumulation, increasing the likelihood of non-uniform plating and surface roughness. Recent studies suggest that modifying surface chemistry to enhance lithiophilicity significantly influences lithium morphology, improving both deposit uniformity and electrochemical performance [20].

In this study, we develop a theoretical framework to describe how lithium redistribution governs metal morphology in electrodeposition. Our model introduces electrochemical Ostwald ripening as a key mechanism in lithium systems, demonstrating its previously unrecognized role in shaping lithium morphology. By elucidating the dynamics of nucleus growth and redistribution, we provide insights into how deposition and cell conditions influence the final structure. Theoretical predictions show excellent agreement with experimental observations across multiple datasets, capturing how nucleus geometry, surface energy, and SEI and electrolyte resistances affect deposit morphology, Coulombic efficiency, and battery longevity. While our analysis focuses on lithium metal anodes, the generality of the model makes it applicable to a wide range of metal electrodeposition processes in electrochemical energy systems.

## Results

### General system description

The morphology of electrodeposited lithium is governed by two competing processes: direct electroplating, and surface energy-driven redistribution. The total overpotential can be defined as the sum of electrodic, diffusive, and surface energy contributions [21]. In the low-current density regime, the electrodic and SEI overpotentials can be linearized and expressed using Ohm's law [21, 22], allowing the total overpotential to be written as:

$$\eta = \frac{i_n}{i_0} \frac{RT}{F} + \frac{i_n r RT}{DC_\infty F^2} + \frac{2\sigma V_m}{Fr} + i_n R_{SEI} S_{tot}, \quad (1)$$

where  $i_n$  is the current density at nucleus surface,  $i_0$  is the exchange current density, and  $F$  is the Faraday constant.  $D$  and  $C_\infty$  are the lithium ion diffusivity and bulk lithium ion concentration of the electrolyte,

respectively.  $R_{SEI}$  is the SEI resistance, and  $S_{tot}$  is the total SEI surface area. The final term,  $\frac{2\sigma V_m}{F r}$ , accounts for the additional overpotential contribution from the surface energy of lithium nuclei.

Since the exchange current density  $i_0$  is relatively high, with characteristic values on the order of  $10^2$ – $10^3$  A/m<sup>2</sup>[23, 24] while the SEI term can vary between  $10^{-1}$  and  $10^3$  cm<sup>2</sup>[25–27], the electrodic overpotential is significant only when the SEI is highly conductive. For simplicity, we combine these two terms into a single corrected SEI resistivity, defined as  $\Re/\kappa = \frac{RT}{i_0 F} + R_{SEI} S_{tot}$ , where  $\kappa$  is a free parameter with units of surface conductance (Ohm<sup>-1</sup>m<sup>-2</sup>) introduced solely for notational convenience.

The current density is related to the rate of change of the nucleus radius as:  $i_n = \frac{3Fv}{V_m s} \frac{dr}{dt}$ , where  $v = \frac{\pi}{3}(2+\cos\theta)(1-\cos\theta)^2$  and  $s = 2\pi(1-\cos\theta)$  are the volumetric and surface shape factors (see Sec.S1). Substituting the dimensionless variables  $\rho = \frac{RT}{2\sigma V_m} r$ ,  $\rho_s = \frac{RT}{F\eta}$ ,  $\tau = \frac{\kappa(RT)^2}{6\sigma F^2} \frac{s}{v} t$ , and  $\omega = \frac{2\sigma V_m \kappa}{DC_\infty F^2}$  into Eq. 1 we obtain:

$$v_\rho = \frac{d\rho}{d\tau} = \frac{1}{\Re + \omega\rho} \left( \frac{1}{\rho_s} - \frac{1}{\rho} \right) \quad (2)$$

Eq. 2 describes the dynamics of the nucleus size evolution. In Fig.1(a), the stationary nucleus radius corresponds to  $\rho_s$  in Eq.2. Following Lifshitz-Slyozov [11], we now introduce the nuclei size distribution function  $f(\rho, \tau)$ . The continuity equation for  $f$  after the nucleation stage is given by

$$\frac{df}{d\tau} + \frac{d}{d\rho} (f v_\rho) = 0 \quad (3)$$

In the constant current regime, mass conservation is expressed as

$$j = \frac{1}{\tau} \int_0^\infty f(\rho, \tau) \rho^3 d\rho = 3 \int_0^\infty f(\rho, \tau) v_\rho \rho^2 d\rho, \quad (4)$$

where  $j = \frac{Fi}{\kappa RT} \frac{3}{s}$  is dimensionless flow.

Equations 2–4 provide a complete description of the system. An interesting consequence of Eq. 2 is the emergence of mixed-dimensional behavior in nuclei growth during Ostwald ripening. At early stages (or under high SEI resistivity conditions,  $\Re \gg \omega\rho$ ), the growth dynamics are governed primarily by SEI resistivity, and the system exhibits an effective dimensionality of  $n = 2$ . In contrast, at later stages (or under low SEI resistivity,  $\omega\rho \gg \Re$ ), the system transitions to behavior consistent with the classical  $n = 3$  dimensional Ostwald ripening equation of motion. Both limits, by choosing the appropriate  $\kappa$  such that  $\Re = 1$  in the 2 dimensional and  $\omega = 1$  in the 3 dimensional case, can be unified into a generalized form

$$v_\rho = \frac{d\rho}{d\tau} = \frac{1}{\rho^{n-1}} \left( \frac{\rho}{\rho_s} - 1 \right). \quad (5)$$

## Asymptotic limits

For high current densities  $j$  or (and) high total charge-transfer resistance, the term  $\frac{1}{\rho_s}$  becomes dominant in  $v_\rho$  and ripening becomes negligible. In this regime, nucleus growth proceeds conserving the nucleus number density. As a result, the size distribution  $f(r, t)$  evolves primarily through a shift in its center—moving toward larger radii in time—while approximately preserving its shape[28], apart from an amplitude correction scaling (see Table1, Sec. S2.1).

By comparing the surface energy term with the charge-transfer resistance and assuming a characteristic nucleus size at nucleation of  $\rho^* \sim 1$  (or  $r^* \sim 18$  nm for lithium), we estimate that this no-ripening regime occurs when the total charge-transfer resistance satisfies  $(\Re + \omega)/\kappa \gg \frac{RT}{iF} \approx 26 \Omega \cdot \text{cm}^2$  for  $i = 1$  mA/cm<sup>2</sup> at 300 K. Given that SEI resistance is often relatively low, this analysis suggests that ripening is likely active under most practical conditions and becomes even more prominent at elevated temperatures, which indirectly was observed in Ref [25].

Another asymptotic behavior emerges in the limit  $\tau \rightarrow \infty$ . In this regime, the system's behavior depends on the dimensionality  $n$ . In the 3D ripening regime (low SEI resistance), the size distribution narrows over time and ultimately collapses into a delta function (see  $f_{3D}^\infty$  in Tab.1, and Sec. S2.3). This behavior is well known and has been described in galvanic metal deposition without SEI [4].

In both scenarios, the nuclei density  $N$  remains constant, and the mean nucleus volume grows linearly with time,  $\langle \rho^3 \rangle \sim j\tau$ [29]. Experimentally, this is often observed as narrowing of the size distribution at later stages of metal deposition[30].

Table 1: Asymptotic behavior of nucleation density  $N(t)$ , characteristic nucleus radius  $r(t)$ , and distribution function  $f(r, t)$  under different growth regimes ( $c = \frac{V_m}{vNF}$ ). For detailed derivations, see Sec. S2.

Conditions	$N(t)$	$r(t)$	$f(r, t)$
No ripening:			
$(\Re + \omega)/\kappa \gg \frac{RT}{iF}$	$N \approx \text{const}$	$r \sim \sqrt[3]{it}$	$f \approx f_0(r_0) \left(\frac{r}{r_0}\right)^{n-2}, \quad r_0^{n-1} = r^{n-1} - (cit)^{\frac{n-1}{3}}$
3D ripening:			
$\Re \ll \omega\rho$	$N \approx \text{const}$	$r \sim \sqrt[3]{it}$	$f_{3D}^\infty = N\delta(r - \sqrt[3]{cit})$
2D ripening:			
$\Re \gg \omega\rho$	$N \sim i/\sqrt{t}$	$r \sim \sqrt{t}$	$f_{2D}^\infty = 5.19j \frac{\rho}{(\sqrt{2\tau}-\rho)^3} \exp\left(\frac{\sqrt{2\tau}}{\rho-\sqrt{2\tau}}\right)$

For 2D regime the distribution function takes the self-similar form and becomes independent of the initial distribution (see Tab.1, and Sec. S2.2). The nuclei density similarly does not depend on the initial nucleation density and follows the relation:

$$N \approx 1.35 \frac{j}{\sqrt{\tau}} (\rho/r)^2 \approx 2.48 \frac{F^2}{V_m^2} \left( \frac{R_{SEI} S_{tot}}{\sigma} \frac{1}{s} \right)^{\frac{3}{2}} \frac{i\sqrt{v}}{\sqrt{t}}, \quad (6)$$

while the mean nucleus size depends only on  $\tau$ , given by

$$\langle r \rangle \approx 0.844\sqrt{\tau}(r/\rho) \approx 0.689 \frac{V_m}{F} \sqrt{\frac{t\sigma}{R_{SEI} S_{tot}}} \frac{s}{v}. \quad (7)$$

To compare with experimental data, the apparent nucleus size should be rescaled as  $r_{\text{apparent}} = \alpha r$ , where  $\alpha = \sin\theta$  for contact angles  $\theta < 90^\circ$  and  $\alpha = 1$  for  $\theta \geq 90^\circ$  (Fig. 1(b)). Notably, in this limit, the expected nucleus radius is independent of the current density and is entirely determined by the metal surface energy and  $R_{SEI}$ , while increasing the current only affects the nuclei density  $N$ . In comparison to the 3D regime, the nuclei density  $N$  decreases with time, which ensures faster growth of the nucleus size  $r$  at the same current (Fig.2(a,b)). Additionally, the growth rate depends on the metal/electrode contact angle  $\theta$ , which determines the nucleus surface-to-volume ratio. The growth rate reaches its minimal value at  $\theta = 120^\circ$  (Fig.2(c,d)), as the smaller contact angles ensure denser lithium plating and larger nucleus sizes [18].

As the system transitions from the 2D to the 3D regime, the nucleus size distribution undergoes a distinct transformation. Initially, in the 2D regime, the distribution broadens, leading to a wide range of nucleus sizes (left part of Fig.2(e)). However, as the system evolves and bulk electrolyte diffusion becomes more dominant, the distribution gradually narrows (right part of Fig.2(e)). This transition occurs as the resistance associated with the SEI layer becomes less significant compared to bulk diffusion, allowing for more homogeneous growth. In the 3D regime, the growth dynamics favor a more uniform expansion of nuclei, and in the asymptotic limit, the distribution approaches a delta function, characteristic of classical diffusion-controlled deposition.

The characteristic moment of regime switching can be estimated from the condition  $\rho_{sw}\omega = \Re$ . In lithium batteries it is estimated to range from 100  $\mu\text{m}$  to 10 mm, based on values of  $R_{SEI}$  and  $D$  from Refs. [9, 27, 31]. However, this range appears unreasonably large compared to the characteristic feature sizes typically observed in electrode morphology studies (which are usually on the order of  $\sim 10^0 - 10^1 \mu\text{m}$ ). As a result, the switching process is expected to occur far beyond the model's applicability — when the electrode surface is nearly fully covered and nuclei can no longer be treated as isolated, but rather as a fused, porous medium.

The nucleus size at this full-coverage point ( $r_{cov}$ ) determines the “weakest point” in the electrode morphology in terms of coverage density, which directly affects battery longevity. In the SEI-passivated column model [16], a simplified approach suggests that the quantity of parasitic side products is approximately proportional to the total exposed metal surface area. As a result, the Coulombic inefficiency,  $1 - \text{CE}$ , can be estimated as being proportional to the nuclei surface-to-volume ratio, i.e.,  $\sim 1/r_{cov}$ . The upper limit of  $r_{cov}$  can be estimated from dense packing as  $\pi\alpha^2 \int_0^\infty f\rho_{cov}^2 d\rho \approx \frac{\pi}{2\sqrt{3}}$ , which in 2D regime corresponds to the time moment  $\alpha^2 \sqrt{\tau_{cov}} \approx 0.278j^{-1}$ . This, in turn, allows us to estimate the characteristic nucleus radius  $r_{cov}$ :

$$t_{cov} \approx 0.0773 \frac{1}{\alpha^4 j^2} (t/\tau) \approx 0.0515 \frac{\sigma}{i^2 R_{SEI} S_{tot}} \frac{vs}{\alpha^4}, \quad (8)$$

$$\langle r_{cov} \rangle \approx 0.844\sqrt{\tau_{cov}}(r/\rho) \approx 0.156 \frac{\sigma V_m s}{Fi R_{SEI} S_{tot} \alpha^2}.$$

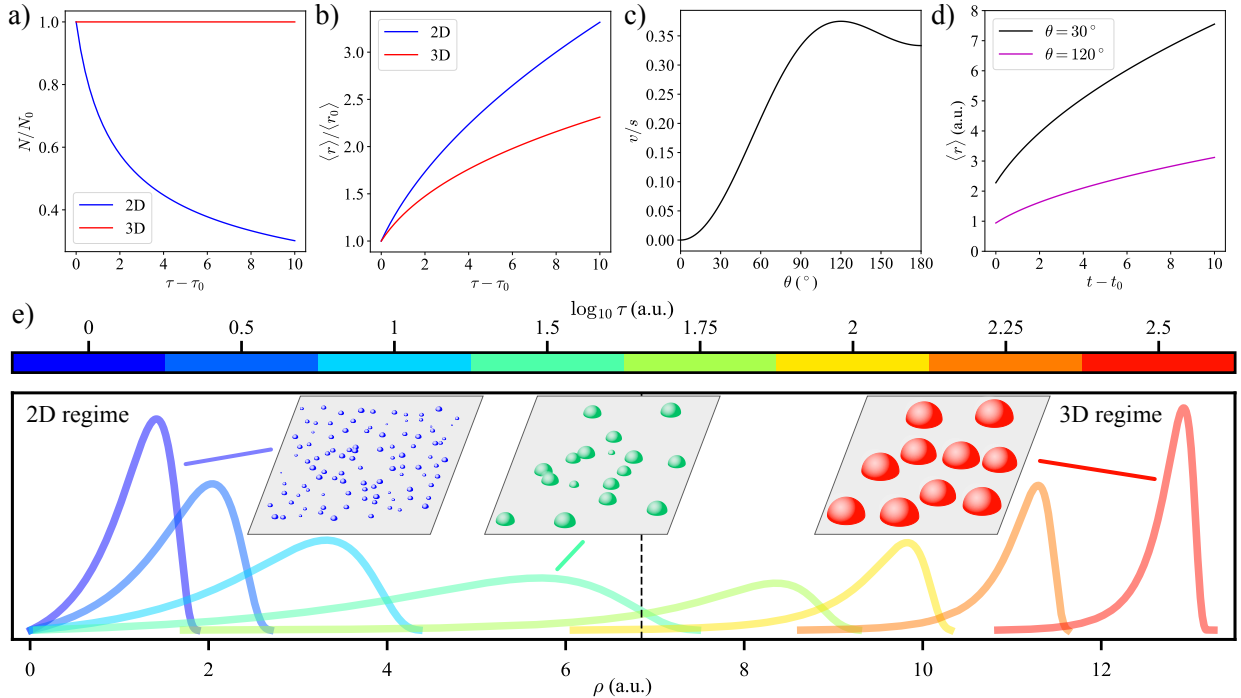


Figure 2: **Comparison of 2D and 3D behavior in constant-current electrochemical Ostwald ripening.** (a) Time evolution of nucleation density ( $N$ ). (b) Time evolution of mean nucleus size ( $\langle r \rangle$ ) in both 2D and 3D regimes. (c) Shape parameter ( $v/s$ ) as a function of contact angle ( $\theta$ ). (d) Comparison of  $\langle r \rangle$  (in units of  $V_m/F\sqrt{\sigma R_{SEI}S_{tot}}$  from Eq. 7) for two different contact angles. (e) Time evolution of the nucleus size distribution: initially following the  $f_{2D}^\infty$  profile, the system gradually transitions to a 3D regime with a narrowing distribution. Different time steps are color-coded; insets illustrate the evolving surface coverage.

It can be seen that, in this model, lower current, SEI resistivity, and contact angle all contribute to a larger  $\langle r_{cov} \rangle$ , resulting in lower surface area exposure, higher CE, and better cycling stability — consistent with experimental observations [18, 25]. While nucleation overpotential (NOP) is often highlighted as a key determinant of battery longevity, it does not explicitly appear in our framework. Nevertheless, we imply that NOP is indirectly governed by nucleus geometry: lower  $\theta$  results in wider nuclei and higher electrode surface coverage for the same deposited lithium volume, which reduces local current densities at nuclei surfaces  $i_n$ . Lower  $i_n$  subsequently decreases the overpotential, promoting formation of a more conductive SEI and reducing the final SEI resistivity ( $R_{SEI}$ ) [32, 33].

## Comparison with experiments

Our predictions align qualitatively with previous experimental observations, particularly regarding the effects of SEI resistivity on nucleus size,  $\langle r_{cov} \rangle$ , and, consequently, battery longevity. In addition, the observed decrease in nucleation density [9] is predicted by our approach, but cannot be explained by the standard nucleation-and-growth model [29]. To further validate our model, we directly compared its quantitative predictions with experimental data. Unfortunately, there are not many studies that investigate all aspects required for comparison with the models result. We identified two studies [9, 25] that provide extensive experimental data, making quantitative validation possible. Both studies used a 1M LiTFSI in DOL/DME electrolyte, with one varying cell temperature [9] and the other varying current density and deposited charges [25].

One of the most challenging aspects of experimental interpretation is determining the correct value of  $R_{SEI}$ . Standard electrochemical impedance spectroscopy (EIS) cannot distinguish  $R_{SEI}$  from other resistive elements in the equivalent circuit [27], leading to significant discrepancies. The true value of  $R_{SEI}$  can be several orders of magnitude lower than the total charge transfer resistance measured by EIS. For example, in a 1M LiPF6 in EC/EMC electrolyte,  $R_{SEI}$  measured under blocking conditions is  $1.5 \Omega \cdot \text{cm}^2$  [27], whereas conventional EIS reports a total resistance of approximately  $100 \Omega \cdot \text{cm}^2$  [26]. To minimize this inconsistency, we assumed that

$R_{SEI}$  follows an Arrhenius relation,  $R_{SEI} = A \exp\left(\frac{E_A}{RT}\right)$ , where  $E_A$  was fitted to experimental data ( $E_A = 32$  kJ/mol, see Fig.S4), leaving  $A$  as the only free parameter in our model. This approach yielded consistent and reproducible results, independently converging to  $R_{SEI} \approx 0.27 \Omega\cdot\text{cm}^2$  at  $300 \text{ K}^1$  for both referenced studies[9, 25].

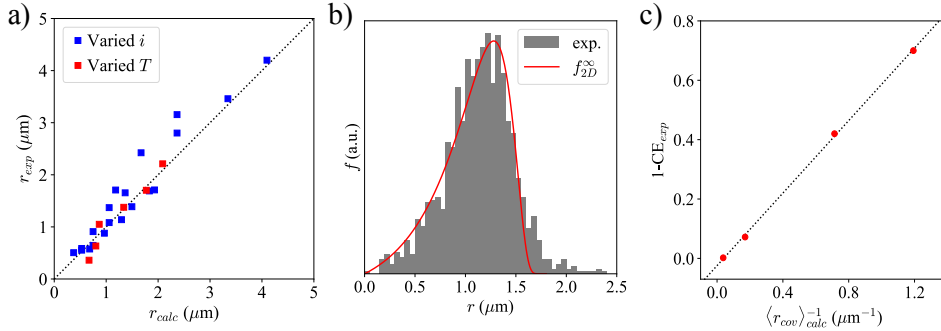


Figure 3: **Comparison of model predictions (Eqs.6-8) with experimental data.** (a, red squares): Nucleus radius observed at different temperatures  $T$  [25]. Variations in temperature affect  $R_{SEI}$ . For  $-10$ ,  $10$ , and  $30^\circ\text{C}$ , the data were calculated from the Arrhenius fit of measured values (see Section S3). (a, blue squares) Comparison of  $r$  obtained for different current densities  $i$  and deposited charges [9]. (b) Bars: size distribution of nuclei extracted from a large SEM image (Fig.S6(a)[9]); red line: nuclei distribution  $f_{2D}^\infty$  (Tab.1). (c) Experimentally measured coulombic inefficiency (1-CE) [25] vs calculated  $1/r_{cov}$  (Eq. 8)

Our model shows excellent agreement with experimentally observed nucleus sizes (Fig.3(a)). The nucleus size distribution captures the characteristic tail in the small-nucleus region (Fig.3(b)), while the elongated tail in the large-nucleus region is likely a result of coalescence effects[34]. Notably, we emphasize the clear linear correlation between Coulombic inefficiency (1-CE) and the inverse of the calculated characteristic radius at the point of full electrode coverage,  $1/r_{cov}$  (Fig. 3(c)). This agreement reinforces the accuracy of our predictions and validates the model’s ability to describe lithium growth dynamics. The strong correlation between theoretical and experimental results suggests that SEI resistance and the metal/electrode contact angle are the key physical factors governing metal morphology. Overall, these findings highlight the reliability of our model and its potential for predicting metal electrodeposition behavior, including lithium plating in battery systems.

## Summary & Conclusion

In this work, we developed a theoretical framework to describe how lithium electrode morphology evolves under the competing influences of electroplating and surface energy–driven redistribution. Our model captures the emergence of variable dimensionality behavior, showing how the system transitions from a surface-resistance-limited 2D regime to a bulk-diffusion-controlled 3D regime over time.

We identified key asymptotic behaviors: at low charge-transfer resistance and current densities, Ostwald ripening dominates, leading to broader size distributions and lower nucleation densities. In contrast, at high currents and total charge-transfer resistance, ripening becomes negligible and all nuclei volume grow at the same rate without material redistribution. In both regimes, the contact angle plays a critical role by modulating nucleus shape and surface-to-volume ratio. Additionally, reducing the contact angle not only lowers the effective NOP and  $R_{SEI}$  but also accelerates the ripening process.

Another important outcome of our model is the prediction of the characteristic nucleus radius ( $r_{cov}$ ) and the time point ( $t_{cov}$ ) at which the electrode surface becomes nearly fully covered. This value correlates with Coulombic efficiency (CE), following the relation  $1 - \text{CE} \sim 1/r_{cov}$ . These results provide a useful framework for understanding how parameters such as current density, SEI resistance, and electrode wettability influence lithium plating density, CE, and overall battery longevity.

Finally, we validated our theoretical predictions against two independent experimental datasets, showing excellent agreement in terms of nucleus size, density, and distribution and Coulombic efficiency.

Based on our findings, we suggest the following strategies for battery performance optimization:

<sup>1</sup>This value likely underestimates  $R_{SEI}$  due to the omission of small nuclei in the original size histograms. While this discrepancy has a negligible effect on the  $\langle r \rangle$ , it can lead to an overestimation of  $\langle r^3 \rangle$ , and thus an underestimation of  $N$  by up to a factor of five.

- Employ electrode materials with a lower metal/electrode contact angle ( $\theta$ ), thereby enhancing electrode wettability and increasing surface coverage. This reduces local current density, nucleation overpotential (NOP), and SEI resistivity, leading to smoother and denser lithium deposits and improved Coulombic efficiency.
- Minimize SEI resistance ( $R_{SEI}$ ) by carefully selecting electrolyte compositions, optimizing formation protocols, and controlling cell operating temperatures. Lowering SEI resistivity facilitates the ripening process, significantly enhancing plating density and battery cycling stability.
- Utilize the lowest practical current density before reaching time  $t_{cov}$  to maximize the characteristic radius  $r_{cov}$ . A larger  $r_{cov}$  corresponds to a lower nucleus surface-to-volume ratio, directly enhancing the battery's Coulombic efficiency and lifespan.

Although our study focused on lithium metal, the underlying principles apply broadly to metal electrodeposition systems where surface morphology plays a critical role. We anticipate that the analytical model presented here will support more precise optimization of battery parameters, ultimately contributing to improved battery performance and lifetime.

## References

- [1] Jingxu Zheng et al. "Regulating electrodeposition morphology of lithium: towards commercially relevant secondary Li metal batteries". In: *Chem. Soc. Rev.* 49 (9 2020), pp. 2701–2750. DOI: 10.1039/C9CS00883G. URL: <http://dx.doi.org/10.1039/C9CS00883G>.
- [2] Albina Jetybayeva et al. "Critical review on recently developed lithium and non-lithium anode-based solid-state lithium-ion batteries". In: *Journal of Power Sources* 566 (2023), p. 232914. ISSN: 0378-7753. DOI: <https://doi.org/10.1016/j.jpowsour.2023.232914>. URL: <https://www.sciencedirect.com/science/article/pii/S0378775323002896>.
- [3] Charles Monroe and John Newman. "Dendrite Growth in Lithium/Polymer Systems : A Propagation Model for Liquid Electrolytes under Galvanostatic Conditions". In: *Journal of The Electrochemical Society* 150.10 (Sept. 2003), A1377. DOI: 10.1149/1.1606686. URL: <https://dx.doi.org/10.1149/1.1606686>.
- [4] Nicholas M. Schneider et al. "Nanoscale evolution of interface morphology during electrodeposition". In: *Nature Communications* 8 (1 Dec. 2017), p. 2174. ISSN: 2041-1723. DOI: 10.1038/s41467-017-02364-9. URL: <https://www.nature.com/articles/s41467-017-02364-9>.
- [5] Johanna K. Stark, Yi Ding, and Paul A. Kohl. "Nucleation of Electrodeposited Lithium Metal: Dendritic Growth and the Effect of Co-Deposited Sodium". In: *Journal of The Electrochemical Society* 160.9 (June 2013), p. D337. DOI: 10.1149/2.028309jes. URL: <https://dx.doi.org/10.1149/2.028309jes>.
- [6] Guangxia Feng et al. "Progressive and instantaneous nature of lithium nucleation discovered by dynamic and operando imaging". In: *Science Advances* 9 (21 May 2023). ISSN: 2375-2548. DOI: 10.1126/sciadv.adg6813. URL: <https://www.science.org/doi/10.1126/sciadv.adg6813>.
- [7] K.C Russell. "Grain boundary nucleation kinetics". In: *Acta Metallurgica* 17 (8 Aug. 1969), pp. 1123–1131. ISSN: 00016160. DOI: 10.1016/0001-6160(69)90057-1. URL: <https://linkinghub.elsevier.com/retrieve/pii/0001616069900571>.
- [8] David R. Ely and R. Edwin García. "Heterogeneous Nucleation and Growth of Lithium Electrodeposits on Negative Electrodes". In: *Journal of The Electrochemical Society* 160 (4 Feb. 2013), A662–A668. ISSN: 0013-4651. DOI: 10.1149/1.057304jes. URL: <https://iopscience.iop.org/article/10.1149/1.057304jes>.
- [9] Allen Pei et al. "Nanoscale Nucleation and Growth of Electrodeposited Lithium Metal". In: *Nano Letters* 17 (2 Feb. 2017), pp. 1132–1139. ISSN: 1530-6984. DOI: 10.1021/acs.nanolett.6b04755. URL: <https://pubs.acs.org/doi/10.1021/acs.nanolett.6b04755>.
- [10] Kang Yan et al. "Temperature-Dependent Nucleation and Growth of Dendrite-Free Lithium Metal Anodes". In: *Angewandte Chemie* 131 (33 Aug. 2019), pp. 11486–11490. ISSN: 0044-8249. DOI: 10.1002/ange.201905251. URL: <https://onlinelibrary.wiley.com/doi/10.1002/ange.201905251>.
- [11] I.M. Lifshitz and V.V. Slyozov. "The kinetics of precipitation from supersaturated solid solutions". In: *Journal of Physics and Chemistry of Solids* 19 (1-2 Apr. 1961), pp. 35–50. ISSN: 00223697. DOI: 10.1016/0022-3697(61)90054-3. URL: <https://linkinghub.elsevier.com/retrieve/pii/0022369761900543>.

- [12] Carl Wagner. “Theorie der Alterung von Niederschlägen durch Umlösen (Ostwald-Reifung)”. In: *Zeitschrift für Elektrochemie, Berichte der Bunsengesellschaft für physikalische Chemie* 65.7-8 (1961), pp. 581–591. DOI: <https://doi.org/10.1002/bbpc.19610650704>. eprint: <https://onlinelibrary.wiley.com/doi/pdf/10.1002/bbpc.19610650704>. URL: <https://onlinelibrary.wiley.com/doi/abs/10.1002/bbpc.19610650704>.
- [13] Peter L. Redmond, A. J. Hallock, and Louis E. Brus. “Electrochemical Ostwald Ripening of Colloidal Ag Particles on Conductive Substrates”. In: *Nano Letters* 5 (1 Jan. 2005), pp. 131–135. ISSN: 1530-6984. DOI: 10.1021/nl048204r. URL: <https://pubs.acs.org/doi/10.1021/nl048204r>.
- [14] Lin Geng et al. “In situ observation of electrochemical Ostwald ripening during sodium deposition”. In: *Nano Research* 15 (3 Mar. 2022), pp. 2650–2654. ISSN: 1998-0124. DOI: 10.1007/s12274-021-3861-6. URL: <https://link.springer.com/10.1007/s12274-021-3861-6>.
- [15] Hyunsik Hwang, Hyuncheol Oh, and Hyunjoon Song. “Shaping Copper Oxide Layers on Gold Nanoparticle Ensembles by Controlled Electrodeposition with Single Particle Scatterometry”. In: *Small* 19 (32 Aug. 2023). ISSN: 1613-6810. DOI: 10.1002/sml1.202301241. URL: <https://onlinelibrary.wiley.com/doi/10.1002/sml1.202301241>.
- [16] Robert M. Kasse et al. “Understanding additive controlled lithium morphology in lithium metal batteries”. In: *J. Mater. Chem. A* 8 (33 2020), pp. 16960–16972. DOI: 10.1039/D0TA06020H. URL: <http://dx.doi.org/10.1039/D0TA06020H>.
- [17] Nicola Boaretto et al. “Lithium solid-state batteries: State-of-the-art and challenges for materials, interfaces and processing”. In: *Journal of Power Sources* 502 (2021), p. 229919. ISSN: 0378-7753. DOI: <https://doi.org/10.1016/j.jpowsour.2021.229919>. URL: <https://www.sciencedirect.com/science/article/pii/S0378775321004511>.
- [18] Lang Ye et al. “Guided lithium nucleation and growth on lithiophilic tin-decorated copper substrate”. In: *Journal of Energy Chemistry* 74 (Nov. 2022), pp. 412–419. ISSN: 20954956. DOI: 10.1016/j.jechem.2022.07.027. URL: <https://linkinghub.elsevier.com/retrieve/pii/S2095495622004077>.
- [19] Rui Zhang et al. “Lithiophilic Sites in Doped Graphene Guide Uniform Lithium Nucleation for Dendrite-Free Lithium Metal Anodes”. In: *Angewandte Chemie International Edition* 56.27 (2017), pp. 7764–7768. DOI: <https://doi.org/10.1002/anie.201702099>. eprint: <https://onlinelibrary.wiley.com/doi/pdf/10.1002/anie.201702099>. URL: <https://onlinelibrary.wiley.com/doi/abs/10.1002/anie.201702099>.
- [20] Kostiantyn V. Kravchyk, Huanyu Zhang, and Maksym V. Kovalenko. “On the interfacial phenomena at the Li<sub>7</sub>La<sub>3</sub>Zr<sub>2</sub>O<sub>12</sub> (LLZO)/Li interface”. In: *Communications Chemistry* 7 (1 Nov. 2024), p. 257. ISSN: 2399-3669. DOI: 10.1038/s42004-024-01350-9. URL: <https://www.nature.com/articles/s42004-024-01350-9>.
- [21] J.L. Barton and J.O’M. Bockris. “The electrolytic growth of dendrites from ionic solutions”. In: *Proceedings of the Royal Society of London. Series A. Mathematical and Physical Sciences* 268 (1335 Aug. 1962), pp. 485–505. ISSN: 0080-4630. DOI: 10.1098/rspa.1962.0154. URL: <https://royalsocietypublishing.org/doi/10.1098/rspa.1962.0154>.
- [22] Michael Hess. “Non-linearity of the solid-electrolyte-interphase overpotential”. In: *Electrochimica Acta* 244 (Aug. 2017), pp. 69–76. ISSN: 00134686. DOI: 10.1016/j.electacta.2017.05.017. URL: <https://linkinghub.elsevier.com/retrieve/pii/S0013468617309891>.
- [23] Ruhul Amin and Ilias Belharouk. “Part I: Electronic and ionic transport properties of the ordered and disordered LiN<sub>0.5</sub>Mn<sub>1.5</sub>O<sub>4</sub> spinel cathode”. In: *Journal of Power Sources* 348 (Apr. 2017), pp. 311–317. ISSN: 03787753. DOI: 10.1016/j.jpowsour.2017.02.071. URL: <https://linkinghub.elsevier.com/retrieve/pii/S0378775317302458>.
- [24] Liulin Que and Wei Chen. “Analysis of the lithium electrodeposition behavior in the charge process of lithium metal battery associated with overpotential”. In: *Journal of Power Sources* 557 (Feb. 2023), p. 232536. ISSN: 03787753. DOI: 10.1016/j.jpowsour.2022.232536. URL: <https://linkinghub.elsevier.com/retrieve/pii/S0378775322015130>.
- [25] Jiangyan Wang et al. “Improving cyclability of Li metal batteries at elevated temperatures and its origin revealed by cryo-electron microscopy”. In: *Nature Energy* 4 (8 July 2019), pp. 664–670. ISSN: 2058-7546. DOI: 10.1038/s41560-019-0413-3. URL: <https://www.nature.com/articles/s41560-019-0413-3>.

- [26] Gustavo M. Hobold, Kyeong-Ho Kim, and Betar M. Gallant. “Beneficial vs. inhibiting passivation by the native lithium solid electrolyte interphase revealed by electrochemical Li + exchange”. In: *Energy & Environmental Science* 16 (5 2023), pp. 2247–2261. ISSN: 1754-5692. DOI: 10.1039/D2EE04203G. URL: <https://xlink.rsc.org/?DOI=D2EE04203G>.
- [27] Sophie Solchenbach et al. “Monitoring SEI Formation on Graphite Electrodes in Lithium-Ion Cells by Impedance Spectroscopy”. In: *Journal of The Electrochemical Society* 168 (11 Nov. 2021), p. 110503. ISSN: 0013-4651. DOI: 10.1149/1945-7111/ac3158. URL: <https://iopscience.iop.org/article/10.1149/1945-7111/ac3158>.
- [28] J. Bartels et al. “Evolution of cluster size distribution in nucleation and growth processes”. In: *Journal of Non-Crystalline Solids* 136 (3 Dec. 1991), pp. 181–197. ISSN: 00223093. DOI: 10.1016/0022-3093(91)90489-S. URL: <https://linkinghub.elsevier.com/retrieve/pii/002230939190489S>.
- [29] Benjamin Scharifker and Graham Hills. “Theoretical and experimental studies of multiple nucleation”. In: *Electrochimica Acta* 28 (7 July 1983), pp. 879–889. ISSN: 00134686. DOI: 10.1016/0013-4686(83)85163-9. URL: <https://linkinghub.elsevier.com/retrieve/pii/0013468683851639>.
- [30] J. L. Fransaer and R. M. Penner. “Brownian Dynamics Simulation of the Growth of Metal Nanocrystal Ensembles on Electrode Surfaces from Solution. I. Instantaneous Nucleation and Diffusion-Controlled Growth”. In: *The Journal of Physical Chemistry B* 103.36 (1999), pp. 7643–7653. DOI: 10.1021/jp990622a. eprint: <https://doi.org/10.1021/jp990622a>. URL: <https://doi.org/10.1021/jp990622a>.
- [31] Chanbum Park et al. “Molecular simulations of electrolyte structure and dynamics in lithium–sulfur battery solvents”. In: *Journal of Power Sources* 373 (2018), pp. 70–78. ISSN: 0378-7753. DOI: <https://doi.org/10.1016/j.jpowsour.2017.10.081>. URL: <https://www.sciencedirect.com/science/article/pii/S0378775317314350>.
- [32] Shengnan Zhang et al. “The lasting impact of formation cycling on the Li-ion kinetics between SEI and the Li-metal anode and its correlation with efficiency”. In: *Science Advances* 10 (3 Jan. 2024), p. 8889. ISSN: 2375-2548. DOI: 10.1126/sciadv.adj8889. URL: <https://www.science.org/doi/10.1126/sciadv.adj8889>.
- [33] Lin Liu and Min Zhu. “Modeling of SEI Layer Growth and Electrochemical Impedance Spectroscopy Response using a Thermal-Electrochemical Model of Li-ion Batteries”. In: *ECS Transactions* 61 (27 Oct. 2014), pp. 43–61. ISSN: 1938-5862. DOI: 10.1149/06127.0043ecst. URL: <https://iopscience.iop.org/article/10.1149/06127.0043ecst>.
- [34] Anthony V. Teran, Andreas Bill, and Ralf B. Bergmann. “Time-evolution of grain size distributions in random nucleation and growth crystallization processes”. In: *Phys. Rev. B* 81 (7 Feb. 2010), p. 075319. DOI: 10.1103/PhysRevB.81.075319. URL: <https://link.aps.org/doi/10.1103/PhysRevB.81.075319>.
- [35] Kenneth Kroenlein et al. *NIST/TRC Web Thermo Tables (WTT) NIST Standard Reference Subscription Database 3 - Professional Edition Version 2*. en. 2011-04-04 2011.

# Supplementary Information: A Predictive Theory of Electrochemical Ostwald Ripening for Electrodeposited Lithium Metal

Hanning Zhang<sup>†</sup>, Oleg V. Yazyev<sup>†</sup>, and Ruslan Yamaletdinov<sup>†,\*</sup>

<sup>†</sup>Institute of Physics, Ecole Polytechnique Fédérale de Lausanne (EPFL), CH-1015 Lausanne, Switzerland

## Contents

<b>S1 Units and quantities</b>	<b>S1</b>
<b>S2 Solution for electrochemical Ostwald ripening</b>	<b>S2</b>
S2.1 No ripening . . . . .	S2
S2.2 The 2D ripening case . . . . .	S3
S2.3 The 3D ripening case . . . . .	S7
<b>S3 Arrhenius fit of <math>R_{SEI}</math> extracted from Ref [25]</b>	<b>S9</b>

## S1 Units and quantities

- $\theta$  - metal/electrode contact angle
- $s = 2\pi(1 - \cos\theta)$  - nucleus surface coefficient. exposed nucleus surface is  $sr^2$
- $v = \frac{\pi}{3}(2 + \cos\theta)(1 - \cos\theta)^2$  - nucleus volumetric coefficient. Total nucleus volume  $vr^3$
- $\sigma$  - metal/electrolyte surface energy. For lithium  $\sigma = 1.716 \text{ J/m}^2$  [3]
- $V_m$  - metal's molar volume. For lithium  $V_m = 13 \text{ cm}^3/\text{mol}$  [35]
- $\Delta G = G_e + \frac{3\sigma V_m}{r}$  - total nucleus free energy,  $G_e$  - environmental Gibbs energy
- $F = 96.485 \text{ s A/mol}$  - Faraday constant
- $\eta$  - overpotential
- $i$  - cell current density
- $i_n$  - current density at nucleus surface
- $i_0$  - electrode exchange current
- CE - Coulombic efficiency
- $R_{SEI}$  - SEI resistance
- $S_{tot}$  - total electrode surface
- $R'_{SEI} = R_{SEI} + \frac{RT}{i_0 F S_{tot}} \approx R_{SEI}$  corrected SEI resistance
- $D$  diffusion coefficient of metal ions in electrolyte
- $C_\infty$  concentration of metal ions in bulk electrolyte
- $\kappa$  surface conductance  $\kappa^{-1} \approx R'_{SEI} S_{tot}$  in the SEI diffusion-limited regime, and  $\kappa^{-1} \approx \frac{2\sigma V_m}{DC F^2}$  in the electrolyte diffusion-limited regime.
- $\mathfrak{R} = \kappa R'_{SEI} S_{tot}$  - dimensionless SEI resistance
- $\omega = \frac{2\sigma V_m \kappa}{DC_\infty F^2}$  - dimensionless electrolyte resistivity
- $N$  - nuclei density
- $r$  - nucleus radius
- $r^* \sim \frac{2\sigma V_m}{RT}$  - critical radius
- $r_{apparent} = \alpha r$  - apparent nucleus radius, where  $\alpha = 1$  for  $\theta \geq 90^\circ$ , and  $\alpha = \sin\theta$  for  $\theta < 90^\circ$
- $\rho = \frac{RT}{2\sigma V_m} r$  - dimensionless radius
- $r_s$  - minimal stable nuclei radius
- $\rho_s = \frac{RT}{F\eta}$  - dimensionless minimal stable nuclei radius
- $r_{cov}$  - the nucleus radius at which the electrode surface becomes completely covered
- $t_{cov}$  - the corresponding timestep
- $f$  - nuclei size distribution function
- $v_\rho = \frac{d\rho}{d\tau}$  - nucleus growth rate
- $\tau = \frac{\kappa(RT)^2}{6\sigma F^2} \frac{s}{v} t$  dimensionless time
- $j = \frac{Fi}{\kappa RT} \frac{3}{s}$  dimensionless flow
- $\nu = N \left( \frac{2\sigma V_m}{RT} \right)^2$  - dimensionless nuclei density

## S2 Solution for electrochemical Ostwald ripening

As outlined in the main text, the evolution of the nucleus size distribution during electrochemical Ostwald ripening is governed by the following system of equations.

The equation of motion

$$v_\rho = \frac{d\rho}{d\tau} = \frac{1}{\rho^{n-1}} \left( \frac{\rho}{\rho_s} - 1 \right), \quad (\text{S1})$$

determines how nuclei with radius  $\rho$  evolve in time. Nuclei smaller than the characteristic radius  $\rho_s$  shrink, while nuclei bigger than the characteristic radius will grow. The evolution of the characteristic radius  $\rho_s$  with time is determined in accordance with the mass conservation Eq.S3.

The continuity equation

$$\frac{df}{d\tau} + \frac{d}{d\rho} (fv_\rho) = 0, \quad (\text{S2})$$

is mathematically equivalent to the equation of motion. The time evolution of individual particles with radius  $\rho$  is rewritten as the time evolution of the radius distribution function  $f$ .

The mass conservation condition under a constant current

$$j\tau = \int_0^\infty f(\rho, \tau) \rho^3 d\rho, \quad \text{or} \quad j = 3 \int_0^\infty f(\rho, \tau) v_\rho \rho^2 d\rho. \quad (\text{S3})$$

corresponds to metal plating when  $j \geq 0$ .

### S2.1 No ripening

In the absence of ripening, we assume  $\rho_s \ll \rho$ , which simplifies the equation of motion (Eq. S1) and yields:

$$\rho^{n-1} = \rho_0^{n-1} + (n-1) \int_0^\tau \frac{d\tau'}{\rho_s(\tau')} = \rho_0^{n-1} + h^{n-1}(\tau), \quad (\text{S4})$$

where  $\rho_0$  is the initial nucleus radius corresponding to a nucleus of size  $\rho$  at time  $\tau$ .

In this regime, the size distribution shifts toward larger  $\rho$  values over time, while conserving the nucleus number density:

$$\nu = \int f(\rho, \tau) d\rho = \int f_0(\rho_0) d\rho_0 = \nu_0 = \text{const},$$

From Eq S4, we have  $d\rho/d\rho_0 = \left(\frac{\rho_0}{\rho}\right)^{n-2}$ , which using  $f(\rho, \tau)d\rho = f_0(\rho_0)d\rho_0$  leads to

$$f(\rho, \tau) = f_0 \left( \sqrt[n-1]{\rho^{n-1} - h^{n-1}(\tau)} \right) \cdot \left( \frac{\rho}{\sqrt[n-1]{\rho^{n-1} - h^{n-1}(\tau)}} \right)^{n-2}. \quad (\text{S5})$$

In 2D, the size distribution remains unchanged in shape and is simply shifted toward larger radii. In contrast, in the 3D case, the distribution becomes narrower, and the function  $f$  assumes bigger values to conserve the total number of nuclei, resulting in a sharper distribution over time.

Mass conservation requires that the total deposited volume equals the integrated current:

$$j\tau = \int_0^\infty f_0(\rho_0) (\rho_0^{n-1} + h(\tau)^{n-1})^{\frac{3}{n-1}} d\rho_0.$$

In the large-time limit, neglecting  $\rho_0$  gives the universal scaling law:

$$\rho \approx h(\tau) \approx \left( \frac{j\tau}{\nu_0} \right)^{1/3}, \quad (\text{S6})$$

## S2.2 The 2D ripening case

Analogously to the Lifshitz–Slyozov approach, we introduce the variable transformation  $z = \rho/\rho_s$  and  $\xi = \ln \rho_s^2$ . Here,  $z$  represents the rescaled nucleus radius, normalized by the evolving characteristic radius  $\rho_s$ , while  $\xi$  taken as the logarithm of the growing characteristic radius  $\rho_s$  acts as the new time variable. Since  $\rho_s \rightarrow \infty$  as  $\tau \rightarrow \infty$ , the asymptote  $\xi \rightarrow \infty$  exists and the asymptotic behavior ( $\tau \rightarrow \infty$  and equivalently  $\xi \rightarrow \infty$ ) of the system will be the focus of the following discussion.

As a first step, we rewrite the equation of motion (Eq. S1) for the 2D case in terms of the rescaled variable  $z$

$$v(z, \gamma) = \frac{\partial z}{\partial \xi} = \gamma \left(1 - \frac{1}{z}\right) - \frac{1}{2}z, \quad (\text{S7})$$

where  $\gamma = \frac{d\tau}{d\rho_s^2}$ . Denoting  $\phi(z, \xi)$  as the new distribution function and preserving the distribution density ( $\phi(z, \xi)dz = f(\rho, \tau)d\rho$ ), the continuity equation (Eq. S2) transforms into

$$\frac{\partial \phi}{\partial \xi} + \frac{\partial}{\partial z}(\phi v_z) = 0. \quad (\text{S8})$$

In the new coordinates ( $z$  and  $\xi$ ) the mass conservation Eq.S3 can be rewritten as

$$j = 3e^{\frac{\xi}{2}} \int_0^\infty (z^2 - z)\phi dz \quad (\text{S9})$$

Interpreting  $\gamma$  as the new  $\rho_s$ , the analogy between Eq. S7, S8, S9 and Eq. S1, S2, S3,  $z$  and  $\rho$  as well as  $\xi$  and  $\tau$  is completed. Indeed  $\rho_s$  and  $\gamma$  both serve as global parameters in the equation of motion and their time evolution  $\gamma(\xi)$  and  $\rho_s(\tau)$  is dictated by the mass conservation condition. The asymptotic limit of  $\gamma(\xi)$  as  $\xi \rightarrow \infty$  is however much more convenient to analyze compared to the limit  $\rho_s(\tau)$  as  $\tau \rightarrow \infty$ , as we will see next.

We begin our discussion with the equation of motion Eq.S7, which governs how individual nuclei evolve over time. The corresponding flow diagram, with  $\gamma$  treated as a free parameter, is shown in Fig.S1. We observe that the diagram can be divided into two different regimes. For  $\gamma < 2$ , all nuclei regardless of their size  $z$  decrease with time  $\xi$ , while for the  $\gamma > 2$  regime, nuclei sizes greater than  $z_- = \gamma - \sqrt{\gamma^2 - 2\gamma}$  (orange line in Fig S1) grow and eventually converge to  $z_+ = \gamma + \sqrt{\gamma^2 - 2\gamma}$  (blue line in Fig S1), while nuclei sizes below the orange line shrink and vanish.

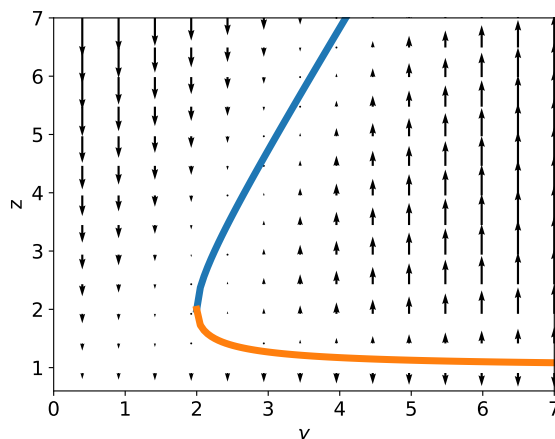


Figure S1: Flow diagram of the rescaled nucleus size  $z$  as governed by Eq. S7. Arrows indicate the direction of  $v(z, \gamma)$  for different values of  $\gamma$ . The orange line denotes the unstable (repelling) fixed point  $z_-$ , while the blue line marks the stable (attracting) fixed point  $z_+$ .

To further fulfill the mass conservation  $\gamma(\xi)$  will evolve as a function of  $\xi$ . We anticipate the result from the following slightly technical proof and state that when  $\gamma < 2$  the dissolution of nuclei is so severe that a constant

current plating cannot be sustained. This prompts  $\gamma$  to increase to values  $\geq 2$ . On the contrary if  $\gamma > 2$ , nuclei will grow too fast leading to a faster than linear current, such the evolution of  $\gamma$  sees it oscillating around the value of 2 with 2 being the only asymptotic value possible.

We start the technical proof by first taking a closer look at the  $\gamma < 2$  case. We define the maximum value of  $v(z)$  as  $v_{max} = \gamma - \sqrt{2\gamma}$ , and  $v_{max} < 0$ . Furthermore  $v(z)$  can be bounded from above by a linear function  $v(z) \leq \gamma - \frac{1}{2}z$  (see Fig S2). As a consequence we write

$$\frac{\partial z}{\partial \xi} = v(z) \leq \gamma - \frac{1}{2}z, v_{max}$$

and nuclei dissolve at least as fast as both, the exponential decay  $z(\xi) \leq 2\gamma + (z_0 - 2\gamma)e^{-\frac{1}{2}\xi}$  and the linear decrease  $z(\xi) \leq z_0 - v_{max}\xi$ , where  $z_0$  is the initial nucleus size at  $\xi = 0$ . Combining both gives a stronger upper bound

$$\frac{\partial z}{\partial \xi} = v(z) \leq \min\{\gamma - \frac{1}{2}z, v_{max}\} < 0$$

which sees nuclei bigger than  $z^*$  dissolving at least exponentially and nuclei smaller than  $z^*$  at least linearly (see FigS2). The nucleus size  $z^*$  is chosen as the intersection of  $v_{max}$  and  $\gamma - \frac{1}{2}z$  and is given by  $z^* = 2\sqrt{2\gamma} > 2\gamma$ .

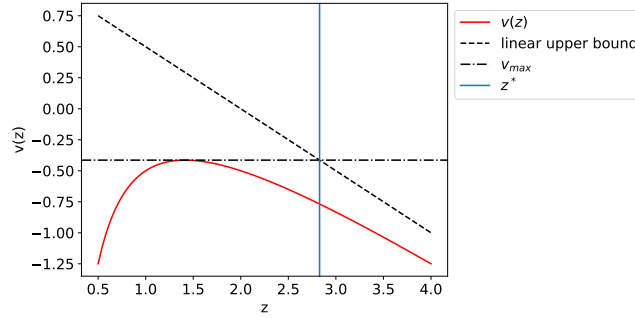


Figure S2: If  $\gamma < 2$ , the function  $v(z)$  can be bounded from above by a constant  $v(z) \leq v_{max}$  and a linear function  $v(z) \leq \gamma - \frac{1}{2}z$ .

We now use this upper bound on the nucleus size, to show that keeping  $\gamma < 2$  effectively leads to a deplating of metal contradicting in particular the constant plating current assumption with  $j \geq 0$ . Let  $\phi_0(z_0)$  denote the initial distribution at  $\xi = 0$  and let  $z(z_0, \xi)$  denote the evolution of an initial nucleus of size  $z_0$  with time. Then

$$j = 3e^{\frac{\xi}{2}} \int_0^{\infty} \phi(z^2 - z) dz = 3e^{\frac{\xi}{2}} \int_0^{\infty} \phi z^2 dz - 3e^{\frac{\xi}{2}} \int_0^{\infty} \phi z dz$$

Since the second integral  $I_2$  is  $\geq 0$ , it is sufficient to show that the first integral  $I_1$  vanishes in the large-time limit. We write

$$I_1 = 3e^{\frac{\xi}{2}} \int_0^{\infty} \phi z^2 dz = 3e^{\frac{\xi}{2}} \int_0^{\infty} \phi_0(z_0) z(z_0, \xi)^2 dz_0 < 3e^{\frac{\xi}{2}} \int_{(z^* - 2\gamma)e^{\frac{1}{2}(\xi - \xi_0)}}^{\infty} \phi_0(z_0) (2\gamma + (z_0 - 2\gamma)e^{-\frac{1}{2}\xi})^2 dz_0.$$

The inequality uses a direct application of the exponential decay upper bound  $v(z) < \gamma - \frac{1}{2}z$  for the integrand, while the lower integration bound additionally subtracts nuclei with initial nucleus size  $z_0$ , which after a time  $\xi$  are completely dissolved. To estimate the lower bound for  $z_0$ , assume that  $\xi_0$  denotes the time to linearly dissolve a nucleus of size  $z^*$ , then the remaining time  $\xi - \xi_0$  can be used to dissolve a nucleus of size of at least  $z_0 = 2\gamma + (z^* - 2\gamma)e^{\frac{1}{2}(\xi - \xi_0)}$  to  $z^*$ . For simplicity the slightly smaller lower bound  $z_0 = (z^* - 2\gamma)e^{\frac{1}{2}(\xi - \xi_0)}$  is then taken.

Expanding

$$\begin{aligned}
& 3e^{\frac{\xi}{2}} \int_{(z^*-2\gamma)e^{\frac{1}{2}(\xi-\xi_0)}}^{\infty} \phi_0(z_0)(2\gamma + (z_0 - 2\gamma)e^{-\frac{1}{2}\xi})^2 dz_0 \\
&= 3e^{\frac{1}{2}\xi} \int_{(z^*-2\gamma)e^{\frac{1}{2}(\xi-\xi_0)}}^{\infty} 2\gamma^2 \phi_0(z_0) dz_0 \\
&+ 3 \int_{(z^*-2\gamma)e^{\frac{1}{2}(\xi-\xi_0)}}^{\infty} 4\gamma(z_0 - 2\gamma)\phi_0(z_0) dz_0 \\
&+ 3e^{-\frac{1}{2}\xi} \int_{(z^*-2\gamma)e^{\frac{1}{2}(\xi-\xi_0)}}^{\infty} 2(z_0 - 2\gamma)^2 \phi_0(z_0) dz_0
\end{aligned}$$

the term with prefactor  $e^{-\frac{1}{2}\xi}$  will go to zero when  $\xi \rightarrow \infty$ . Similarly the term with constant prefactor goes to zero as the lower integration bound approaches infinity (as  $z_0\phi_0(z_0)$  is an integrable function<sup>2</sup>). Finally the term with prefactor  $e^{\frac{1}{2}\xi}$  can be written and upper bounded as

$$Ax \int_{Bx}^{\infty} \phi_0(z_0) dz_0 = \frac{A}{B} Bx \int_{Bx}^{\infty} \phi_0(z_0) z_0 dz_0 < \frac{A}{B} \int_{Bx}^{\infty} \phi_0(z_0) z_0^2 dz_0$$

where  $A = 6\gamma^2$ ,  $B = (z^* - 2\gamma)e^{-\frac{1}{2}\xi_0}$  and  $x = e^{\frac{1}{2}\xi}$ . Since  $\phi_0(z_0)z_0^2$  is an integrable function as well, this term also goes to zero as the lower integration bound goes to infinity. We hence showed that  $\gamma < 2$  needs to increase if a constant plating current needs to be maintained.

Now we turn our attention to the slightly easier  $\gamma > 2$  case. It turns out that asymptotic solutions exists such that  $\gamma$  in principle can stay constant at some value  $> 2$ . The solutions are however unstable, as a perturbation generating a small fraction of nuclei above the orange line  $z_- = \gamma - \sqrt{\gamma^2 - 2\gamma}$ , leads to these nuclei never being dissolved again and growing as  $\rho_s \propto \tau^{1/2}$ . These fast growing nuclei take up more lithium than can be plated by a constant current ( $\tau^{3/2}$  dependence of lithium in these fast growing nuclei versus  $\tau$  dependence of lithium plated by constant current) such that to ensure constant current plating  $\gamma$  will decrease until it reaches a value  $\leq 2$ . We therefore conclude that due to the mass conservation equation  $\gamma$  will evolve towards and asymptotically stabilize at the value  $\gamma = 2$ , as it is the only dynamically consistent solution.

We now derive the time evolution of the nucleus density and the nucleus radius distribution in the asymptotic limit where  $\gamma = 2$ . Note that the  $\gamma$  is kept general until equation Eq. S10 as the same analysis with  $\gamma \neq 2$  will be needed for the 3D analysis.

Introducing:

$$g(z, \gamma) = -v(z, \gamma), \quad \text{and} \quad \psi = \int_0^z g^{-1}(z', \gamma) dz',$$

the general solution of Eq S8 is

$$\phi(z, \tau) = \chi(\xi + \psi) \frac{1}{g(z, \gamma)}$$

The mass conservation Eq.S9 can be rewritten as

$$j = 3e^{\frac{\xi}{2}} \int_0^{\infty} (z^2 - z)\phi dz = 3e^{\frac{\xi}{2}} \int_0^{\infty} (z^2 - z)\chi(\xi + \psi) \frac{1}{g(z, \gamma)} dz.$$

Since the left side is time independent we find that

$$\chi(\xi + \psi) = e^{-\frac{1}{2}(\xi + \psi)}$$

Interestingly, it is at this point that the constant current case deviates from the constant volume 2D Ostwald ripening [12]:

---

<sup>2</sup>The functions  $\phi_0(z_0)z_0^n$  for  $n \in [0, 3]$  is integrable, as these terms correspond to physical quantities such as nuclei density, current, and volume at  $\xi = 0$ , which are assumed to be finite.

$$V = e^{\frac{3\xi}{2}} \int_0^\infty \phi z^3 dz,$$

which leads to

$$\chi(\xi + \psi) = e^{-\frac{3}{2}(\xi + \psi)}.$$

We generalize both cases by writing

$$\phi(z, \xi) = e^{-\alpha\xi} \Phi(z),$$

where  $\alpha = \frac{1}{2}$  in the case of constant current and  $\alpha = \frac{3}{2}$  in the case of constant volume. Substituting this into the continuity equation (Eq. S2) leads to the time-independent form:

$$v \frac{\partial \Phi}{\partial z} + \Phi \frac{\partial v}{\partial z} = \alpha \Phi \quad (\text{S10})$$

Introducing the function  $\beta(z) = \alpha - \frac{dv}{dz}$  and setting  $\gamma = 2$ , we solve the equation using separation of variables:

$$\frac{\beta}{v} dz = \frac{1}{\Phi} d\Phi,$$

which yields the solution:

$$\Phi(z) = \frac{z}{(2-z)^{2(\alpha+1)}} e^{\frac{4\alpha}{z-2}},$$

with the physical requirement that  $\Phi(z) = 0$  for  $z > z_+ = z_- = 2$ . Furthermore, it is straightforward to show that the root  $z_\beta$  of  $\beta(z)$  must satisfy  $z_\beta < z_+ = z_- = 2$  for the solution to be physical. This is equivalent to the condition  $\alpha > 0$ , which holds for both the constant current ( $\alpha = \frac{1}{2}$ ) and constant volume ( $\alpha = \frac{3}{2}$ ) cases.

The final solution for the constant current case is hence

$$\phi(z, \xi) = A \frac{z}{(2-z)^3} \exp\left(\frac{2}{z-2}\right) e^{-\xi/2}, \quad (\text{S11})$$

which, when transformed back to the original variables  $\rho$  and  $\tau$ , yields:

$$f_{2D}^\infty(\rho, \tau) = A \frac{\rho}{(\sqrt{2\tau} - \rho)^3} \exp\left(\frac{\sqrt{2\tau}}{\rho - \sqrt{2\tau}}\right).$$

The conservation of mass Eq. S9, provides a normalization condition for constant current plating

$$j = 3A \int_0^2 (z^2 - z) \frac{z}{(2-z)^3} e^{\frac{2}{z-2}} dz \approx 0.1925A$$

We derive the following important quantities:

- **Nucleation density:**

$$\nu = \int_0^2 \phi(z, \xi) dz = \int_0^\infty f(\rho, \tau) d\rho \approx 0.956 j e^{-\xi/2} \approx 1.35 \frac{j}{\sqrt{\tau}}.$$

- **Mean nucleus radius:**

$$\nu \langle \rho \rangle = \int_0^\infty \rho f(\rho, \tau) d\rho = e^{\xi/2} \int_0^2 z \phi(z, \xi) dz \approx 1.14 j \rightarrow \langle \rho \rangle \approx 0.844 \sqrt{\tau}.$$

- **Mean square radius:**

$$\nu \langle \rho^2 \rangle = \int_0^\infty \rho^2 f(\rho, \tau) d\rho = e^\xi \int_0^2 z^2 \phi(z, \xi) dz \approx 1.47 j e^{\xi/2} \approx 1.04 j \sqrt{\tau} \rightarrow \langle \rho^2 \rangle \approx 0.770 \tau.$$

We emphasize here that the derivation for the constant current case represents, to the best of our knowledge, a new result. Interestingly, the discussion on the asymptotic value of  $\gamma$  is exactly the same as in the constant-volume 2D Ostwald ripening case. This will not remain true for the 3D case. The difference between constant current and constant volume only became apparent in the final calculation of the distribution function  $f$ , where distinct values  $\alpha = \frac{1}{2}$  and  $\alpha = \frac{3}{2}$  were used.

### S2.3 The 3D ripening case

In the 3D case, we again follow the Lifshitz-Slyozov approach [11] and define variables  $z = \rho/\rho_s$  and  $\xi = \ln \rho_s^3$ .

In a first step we rewrite the equation of motion as

$$v(z, \gamma) = \frac{\partial z}{\partial \xi} = \gamma \frac{z-1}{z^2} - \frac{z}{3}, \quad (\text{S12})$$

where  $\gamma = \frac{d\tau}{d\rho_s^3}$ . The continuity equation retains the same form as in Eq. S8, while the mass conservation condition for constant-current 3D ripening becomes

$$j = 3 \int_0^\infty (z-1)\phi(z)dz \quad (\text{S13})$$

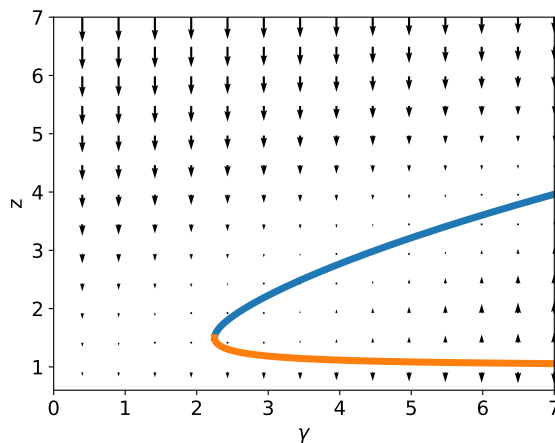


Figure S3: Flow diagram of the rescaled nucleus size  $z$  as governed by Eq. S12. Arrows indicate the direction of  $v(z, \gamma)$  for different values of  $\gamma$ . The orange line denotes the unstable (repelling) fixed point  $z_-$ , while the blue line marks the stable (attracting) fixed point  $z_+$ .

We draw the corresponding flow diagram with  $\gamma$  as a free variable in Fig S3. Similarly to the previously described 2D case, we note that for  $\gamma < 9/4$ , the function  $v(z)$  doesn't have any zeros in the  $z > 0$  region, while for  $\gamma > 9/4$ , it possesses two real zeros corresponding to a repelling  $z_-$  and an attracting fixed point  $z_+$  (orange and blue lines in Fig. S3).

The time evolution of  $\gamma(\xi)$  is described as follows: In the  $\gamma < 9/4$  case, a constant plating current  $j = 3 \int_0^\infty \phi(z)(z-1)dz \geq 0$  can not be maintained since

$$3 \int_0^\infty \phi_0(z_0)z(z_0, \xi)dz_0 < 3 \int_{-v_{max}\xi}^\infty \phi_0(z_0)z_0dz_0 \rightarrow 0,$$

where  $v_{max} < 0$  is the maximum of  $v(z)$ . The line of argumentation closely follows the 2D case, and defines an upper bound for the integrand as  $z(z_0, \xi) < z_0$ , while the lower integration bound accounts for the minimal initial radius  $z_0 > -v_{max}\xi$  that will be dissolved after time  $\xi$ . Showing that  $3 \int \phi(z)zdz \rightarrow 0$  then directly leads to  $j \leq 0$  in the large  $\xi$  limit, such that conversely, perserving the constant current condition forces  $\gamma$  to increase to values  $\geq 9/4$ .

In the  $\gamma > 9/4$  case, any small fraction of nuclei above the orange line  $z_-$  will converge to the blue line  $z_+$ . Contrary to the 2D discussion, this doesn't lead to a contradiction with the mass conservation but indeed, having all nuclei the same size  $z_+$  growing  $\propto \tau^{1/3}$  exactly fulfills the constant current condition. We hence summarize that values  $\gamma < 9/4$  will increase with progressing time  $\xi$ , while all  $\gamma \geq 9/4$  are expected to be physical asymptotes, with their respective asymptotic distribution being derived in the following paragraph.

To obtain the asymptotic distribution we follow the 2D derivation until Eq. S10

$$v \frac{\partial \Phi}{\partial z} + \Phi \frac{\partial v}{\partial z} = \alpha \Phi$$

The corresponding constant current constraint

$$j = 3 \int_0^\infty (z-1)\phi(z)dz = 3e^{-\alpha\xi} \int_0^\infty (z-1)\Phi(z)dz$$

leads to  $\alpha = 0$ . As a side note, we mention here that for the 3D Ostwald ripening with constant volume  $\alpha = 1$ , such that we can obtain the asymptotic distribution by following the 2D discussion verbatim.

For our constant current case

$$\frac{\partial \Phi(z)v(z)}{\partial z} = 0 \tag{S14}$$

and direct integration leads to

$$\Phi(z)v(z) = c$$

with some integration constant  $c$ . Interestingly  $\Phi(z) = \frac{c}{v(z)}$  does not yield a physical result, as  $\frac{1}{v(z)}$  is not normalizable due to divergences at the zeros of  $v(z)$ . Instead, the physical asymptotic distribution is a more subtle solution of Eq. S14 in form of a delta function centered at the attractive fixed point  $z_+$

$$\Phi(z) = A\delta(z - z_+),$$

where  $A$  is a normalization constant. We discard the solution  $\Phi(z) = \delta(z - z_-)$ , because  $z_-$  is a repelling fixed point in the flow diagram (Fig. S3).

We conclude by deriving the following quantities:

- **Nucleation density:**

$$\nu = \int A\delta(z - z_+)dz = A$$

Unlike in the 2D constant-current ripening case, the nucleation density  $\nu$  in 3D remains constant over time and can be treated as an independent variable. The normalization condition, based on mass conservation (Eq. S13), yields:

$$j = 3 \int (z-1)A\delta(z - z_+)dz = 3\nu(z_+ - 1)$$

which gives

$$\gamma = \frac{\nu}{j} \left( \frac{j}{3\nu} + 1 \right)^3,$$

and trivial

- **Nucleus radius:**

$$\rho = \sqrt[3]{\frac{j\tau}{\nu}}$$

We note here that the 3D constant current case strongly deviates from the constant volume 3D Ostwald ripening, which again sees  $\gamma = 9/4$  as the sole possible asymptote. Furthermore, while the constant current case with  $\alpha = 0$  leads to a  $\delta$ -function the constant volume case with  $\alpha = 1$  leads to a non-trivial asymptotic distribution with finite width.

To conclude, we highlight some qualitative differences between the 2D and 3D ripening behaviors that offer further physical intuition. At the level of the original variables  $(\rho, \tau)$ , the growth velocity  $v_\rho$  in 2D increases monotonically with  $\rho$ , meaning that even small perturbations to a  $\delta$ -like distribution cause it to break apart as smaller nuclei dissolve faster. In contrast, the 3D case features a non-monotonic  $v_\rho$  with a maximum at finite  $\rho$ ,

making the  $\delta$ -distribution a stable solution: perturbations tend to self-correct, and the system naturally relaxes back to a narrow distribution.

In the rescaled coordinates  $(z, \xi)$ , this difference manifests in the flow diagram: the unstable  $\delta$ -solution in 2D is hidden in the  $\gamma \rightarrow \infty$  limit below the repelling orange line, whereas the stable  $\delta$ -solution in 3D emerges at  $\gamma \geq 9/4$  and corresponds to the attractive fixed point (blue line).

Finally, we comment on why the constant-volume Ostwald ripening result appears similarly to the constant current case in 2D, but not in 3D. In 2D, the instability of the  $\delta$ -distribution leads both constant-volume and constant-current formulations to converge toward the self-similar asymptotic form. In 3D, however, the physical mechanism underlying volume conservation requires  $\rho_s$  to track the distribution center, while under constant current  $\rho_s$  can lag behind—effectively decoupling the evolution from constant volume ripening and producing qualitatively different dynamics.

### S3 Arrhenius fit of $R_{SEI}$ extracted from Ref [25]

Table S2: Data extracted from Ref [25]. 1M LiTFSI, DOL/DME/LiNO<sub>3</sub>. Current density 0.25 mA cm<sup>-2</sup>, capacity 0.15 mAh cm<sup>-2</sup>.  $vN$  calculated as total capacity divided by  $r^3$

$T$ (°C)	$R_{SEI}$ ( $V_m$ )	$r$ ( $\mu\text{m}$ ) <sup>b</sup>	$vN$ ( $\mu\text{m}^{-2}$ )
-20	224	0.36	15.5
-10	157*	0.63	2.9
0	134	1.1	0.63
10	56*	1.4	0.28
20	32	1.7	0.15
30	23*	2.2	0.067

\* calculated from linear regression in Arrhenius coordinates  $\ln(R) \sim -T^{-1}$

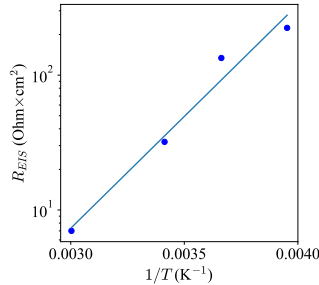


Figure S4: Linear regression of  $R_{SEI}$  in Arrhenius coordinates  $\ln(R) \sim -T^{-1}$

## References

- [3] Charles Monroe and John Newman. “Dendrite Growth in Lithium/Polymer Systems : A Propagation Model for Liquid Electrolytes under Galvanostatic Conditions”. In: *Journal of The Electrochemical Society* 150.10 (Sept. 2003), A1377. DOI: 10.1149/1.1606686. URL: <https://dx.doi.org/10.1149/1.1606686>.
- [11] I.M. Lifshitz and V.V. Slyozov. “The kinetics of precipitation from supersaturated solid solutions”. In: *Journal of Physics and Chemistry of Solids* 19 (1-2 Apr. 1961), pp. 35–50. ISSN: 00223697. DOI: 10.1016/0022-3697(61)90054-3. URL: <https://linkinghub.elsevier.com/retrieve/pii/0022369761900543>.
- [12] Carl Wagner. “Theorie der Alterung von Niederschlägen durch Umlösen (Ostwald-Reifung)”. In: *Zeitschrift für Elektrochemie, Berichte der Bunsengesellschaft für physikalische Chemie* 65.7-8 (1961), pp. 581–591. DOI: <https://doi.org/10.1002/bbpc.19610650704>. eprint: <https://onlinelibrary.wiley.com/doi/pdf/10.1002/bbpc.19610650704>. URL: <https://onlinelibrary.wiley.com/doi/abs/10.1002/bbpc.19610650704>.

- [25] Jiangyan Wang et al. “Improving cyclability of Li metal batteries at elevated temperatures and its origin revealed by cryo-electron microscopy”. In: *Nature Energy* 4 (8 July 2019), pp. 664–670. ISSN: 2058-7546. DOI: 10.1038/s41560-019-0413-3. URL: <https://www.nature.com/articles/s41560-019-0413-3>.
- [35] Kenneth Kroenlein et al. *NIST/TRC Web Thermo Tables (WTT) NIST Standard Reference Subscription Database 3 - Professional Edition Version 2*. en. 2011-04-04 2011.